



# Synergy of nitrogen vacancies and intercalation of carbon species for enhancing sunlight photocatalytic hydrogen production of carbon nitride

Xue Ma, Hefa Cheng<sup>\*</sup>

MOE Key Laboratory for Earth Surface Processes, College of Urban and Environmental Sciences, Peking University, Beijing 100871, China

## ARTICLE INFO

### Keywords:

Photocatalytic hydrogen production  
Exfoliated CN nanosheets  
Nitrogen vacancies  
Carbon intercalation  
Built-in electric field

## ABSTRACT

Enhancing the separation of photogenerated electrons and holes is crucial for improving the photocatalytic performance of carbon nitride (CN). In this work, a ECN-V<sub>N</sub>/C photocatalyst with unique three-dimensional nanostructure was constructed by exfoliation of multilayered CN, followed by introduction of nitrogen vacancies and intercalation of carbon species between the exfoliated CN nanosheets. Compared to pristine CN, ECN-V<sub>N</sub>/C photocatalyst has stronger light absorption, more surface active sites, and better separation efficiency of photogenerated carriers. Formation of dual built-in electric fields in ECN-V<sub>N</sub>/C, which result from the synergy of nitrogen vacancies and intercalation of carbon species, promotes the migration of photogenerated electrons and holes in opposite directions, and greatly accelerates the separation efficiency of these carriers. Photocatalytic hydrogen production activity of ECN-V<sub>N</sub>/C photocatalyst was 12.1 times higher than that of pristine CN. The synergy between nitrogen vacancies and intercalation of carbon species provides a new strategy for designing more efficient CN-based photocatalysts.

## 1. Introduction

To cope with climate change brought by the emissions of greenhouse gases and accelerate the global transition away from fossil energy, development of sustainable and pollution-free renewable energy sources has become a priority [1–3]. Hydrogen is one of the most common and abundant elements on the earth, and its heat energy released from combustion per unit mass is 3 times higher than that of gasoline [4]. It is also environmentally friendly as only water is produced from its combustion. Thus, hydrogen is considered as one of the most promising energy carriers for the future of transportation, and it could be a viable alternative to fossil fuels for meeting future energy demand [5–8]. Hydrogen is mainly produced from steam-methane reforming and coal gasification [9]. Besides the use of fossil fuels as raw materials, these technologies require extreme reaction conditions and are expensive [9]. Recently, photocatalytic water splitting has been developed as the most environmentally friendly and safest way of hydrogen production [10–13]. Driven by the free solar energy, high-efficiency photocatalysts can effectively split water into hydrogen and oxygen, and the production process is sustainable and clean [14–16].

As most semiconductor materials by themselves do not exhibit high photocatalytic activity, development of composite photocatalysts with

good performance in water splitting remains the focus of research [17–20]. Carbon nitride (CN) is one of the most valuable functional polymeric semiconductor materials because of its non-toxic, low-cost, and stable characteristics [21–23]. However, the low quantum efficiency and high recombination rate of photogenerated carriers limit its practical application in photocatalysis [24,25]. There has been plenty of research devoted to improving the photocatalytic performance of CN. Niu et al. prepared a H<sub>2</sub>-reduced CN by heating CN in a hydrogen atmosphere to produce nitrogen vacancies, which exhibited superior photocatalytic activity in degrading Rhodamine B compared to pristine CN [26]. Chen et al. introduced the donor-acceptor (DA) system into CN nanosheets through oxygen and/or phenyl doping strategy (DA-CN), which increased the photocatalytic hydrogen production efficiency by 7.67 times [27]. Wang et al. constructed a direct Z-scheme heterojunction of defective CN/CdS, whose hydrogen production activity was 6.09 times higher than that of pristine CN [28]. These studies demonstrate that the recombination of photo-excited charge carriers in CN can be effectively suppressed by introducing nitrogen vacancies, doping with functional groups, and forming heterojunctions. Although the electronic properties of semiconductors are modified, doping with heteroatoms introduces impurities into the crystal lattice, which may become the recombination centers of photogenerated carriers. In

<sup>\*</sup> Corresponding author.

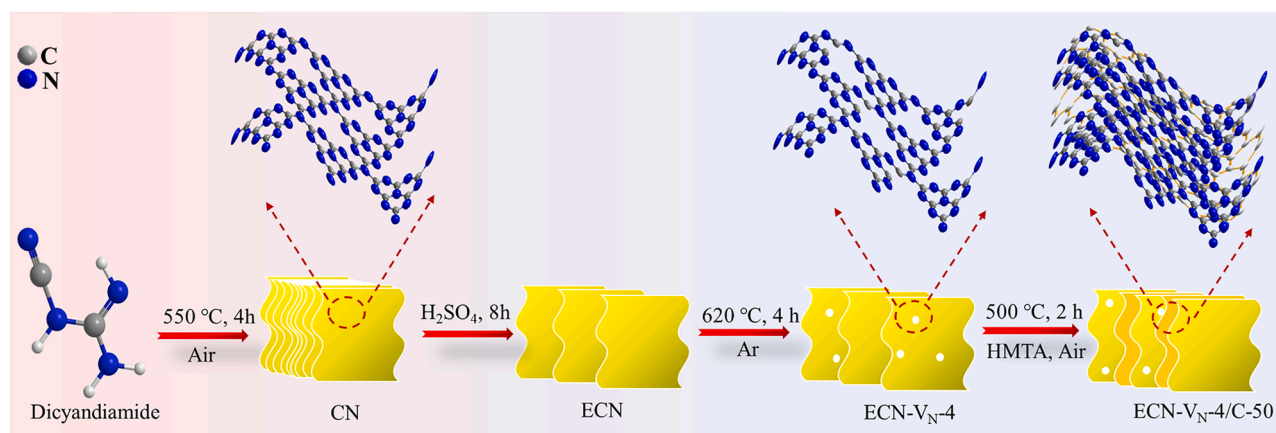
E-mail address: [hefac@umich.edu](mailto:hefac@umich.edu) (H. Cheng).

<https://doi.org/10.1016/j.apcatb.2022.121497>

Received 22 February 2022; Received in revised form 21 April 2022; Accepted 7 May 2022

Available online 11 May 2022

0926-3373/© 2022 Elsevier B.V. All rights reserved.



**Scheme 1.** Overview of the steps involved in the preparation of ECN-V<sub>N</sub>-4/C-50 photocatalyst.

addition, the interface defects formed between different materials due to improper growth can also function as carrier traps and recombination centers, which inhibit electron-hole separation [29].

To maximize the separation of photogenerated carriers, constructing a built-in electric field (BIEF) in the photocatalyst is an effective strategy. The reverse transfer of excited electrons and holes can greatly accelerate the separation rate of photogenerated carriers. In particular, researchers have designed hierarchically structured materials with dual BIEFs to further improve their photocatalytic activity. For examples, Zhao et al. prepared a PdS@CdS@MoS<sub>2</sub> photocatalyst with dual BIEFs near the interface of PdS and CdS, and CdS and MoS<sub>2</sub>, which exhibited significantly enhanced hydrogen production efficiency compared with CdS nanoparticles [30]. Wang et al. constructed a Z-scheme O-g-C<sub>3</sub>N<sub>4</sub>/Zn<sub>2</sub>SnO<sub>4</sub>N/ZnO ternary heterojunction with dual BIEFs at the interfaces, which exhibited enhanced photocatalytic performance for photo-degradation of organic dyes and NO removal compared with O-g-C<sub>3</sub>N<sub>4</sub> and Zn<sub>2</sub>SnO<sub>4</sub>N/ZnO [31]. Kuang et al. fabricated a CdS/Cu<sub>2</sub>O/ZnO ternary nanocomposite, and reported that the dual BIEFs formed allowed fast generation, separation, and transfer of charge carriers in the Cu<sub>2</sub>O/ZnO and Cu<sub>2</sub>O/CdS dual p – n junction regions [32]. The dual BIEFs in these studies were formed between the interfaces of three semiconductor components, and they promoted the transfer of electrons from one semiconductor to another to achieve separation of photogenerated carriers. However, the flow of electrons between semiconductors has to overcome the limitations of contact interfaces and external environment factors (e.g., electronic field and magnetic field).

Here we proposed a new strategy of forming dual BIEFs within CN to promote the separation and transfer of carriers without introducing heteroatoms based on the synergy between nitrogen vacancies and intercalation of carbon species. A high-efficiency photocatalyst was constructed by first exfoliating multilayered CN into thin nanosheets (ECN), followed by introduction of nitrogen vacancies (ECN-V<sub>N</sub>), and intercalation of carbon species between the nanosheets to modify the energy band structure of CN and achieve energy level rearrangement (ECN-V<sub>N</sub>/C). The alignment of the Fermi levels and flow of electrons not only improve the band structure, but also produce a charge imbalance in the direction perpendicular to the interface, which leads to the formation of dual BIEFs at the interfaces between ECN and ECN-V<sub>N</sub>, and between ECN-V<sub>N</sub> and ECN-V<sub>N</sub>/C as well. Establishing BIEFs in the same phase can eliminate the influence of interfacial defects between different materials and obtain higher carrier separation efficiency [29]. At the same time, the dual BIEFs developed in this way are widely distributed within the photocatalyst, which promote faster migration of carriers and improve its conductivity. Thus, the dual BIEFs formed in the same phase is advantageous in enhancing photocatalytic activity compared to the traditional ones created at the interfaces of composites.

In this work, a high-efficiency ECN-V<sub>N</sub>/C photocatalyst for hydrogen

production under simulated sunlight was synthesized by continuous calcination. The energy band structures and work functions of different components in ECN-V<sub>N</sub>/C were investigated by first-principle density functional theory (DFT) calculations. With exfoliation of the multilayered CN into nanosheets of a few layers, introduction of nitrogen vacancies, and even intercalation of carbon species in the interlayer regions, the ECN-V<sub>N</sub>/C photocatalyst prepared had reduced electron transfer distance, expanded light absorption range, and significantly increased active surface area. In addition, the synergy of nitrogen vacancies and intercalation of carbon species results in the formation of dual BIEFs within ECN-V<sub>N</sub>/C, which further facilitate the separation of electron-hole pairs. As a result, ECN-V<sub>N</sub>/C exhibited much greater activity in photocatalytic hydrogen production compared to pristine CN.

## 2. Experimental

### 2.1. Photocatalyst preparation

CN was prepared from dicyandiamide by the commonly used calcination method (550 °C in the air for 4 h) [33]. After cooling, the yellow product obtained was ground into a fine powder. ECN was prepared by the method of chemical exfoliation [34]. Specially, power of CN (1.0 g) was mixed with 10 mL of H<sub>2</sub>SO<sub>4</sub> (98 wt%) under continuous stirring for 8 h. Then the mixture was slowly poured into 100 mL of ultrapure water, and sonicated to assist CN exfoliation. The resulting suspension was thoroughly washed and centrifuged, and finally dried at 60 °C for 12 h. The obtained product was ground into a fine powder.

ECN with nitrogen vacancies (ECN-V<sub>N</sub>-x, where x represents the hours of calcination) was prepared by the method of calcination [35]. For the engineering of nitrogen vacancies, the as-obtained ECN was calcinated in an argon atmosphere at 620 °C for 2, 4, and 6 h, respectively. The ECN-V<sub>N</sub>-x samples obtained were ground into fine powders.

The synthesis route for ECN-V<sub>N</sub>-4/C-y (where y corresponds to the mass of hexamethylenetetramine (HMTA) used) is shown on Scheme 1. Pre-determined doses of HMTA (30, 50, 70, and 90 mg, respectively) were uniformly mixed with 1.0 g of ECN-V<sub>N</sub>-4, and then calcinated at 500 °C for 2 h [36]. Carbon species produced from the sublimation and thermal degradation of HMTA could easily enter the interlayer regions of ECN-V<sub>N</sub>-4 [36]. After cooling, the light brown carbon-rich ECN-V<sub>N</sub>-4/C-y photocatalysts obtained were fully ground into fine powders.

### 2.2. Sample characterization

Powder X-ray diffraction (XRD, PANalytical, X-Pert3 Powder), field-emission scanning electron microscopy (SEM, ZEISS, Merlin Compact), field-emission high resolution transmission electron microscopy (TEM,

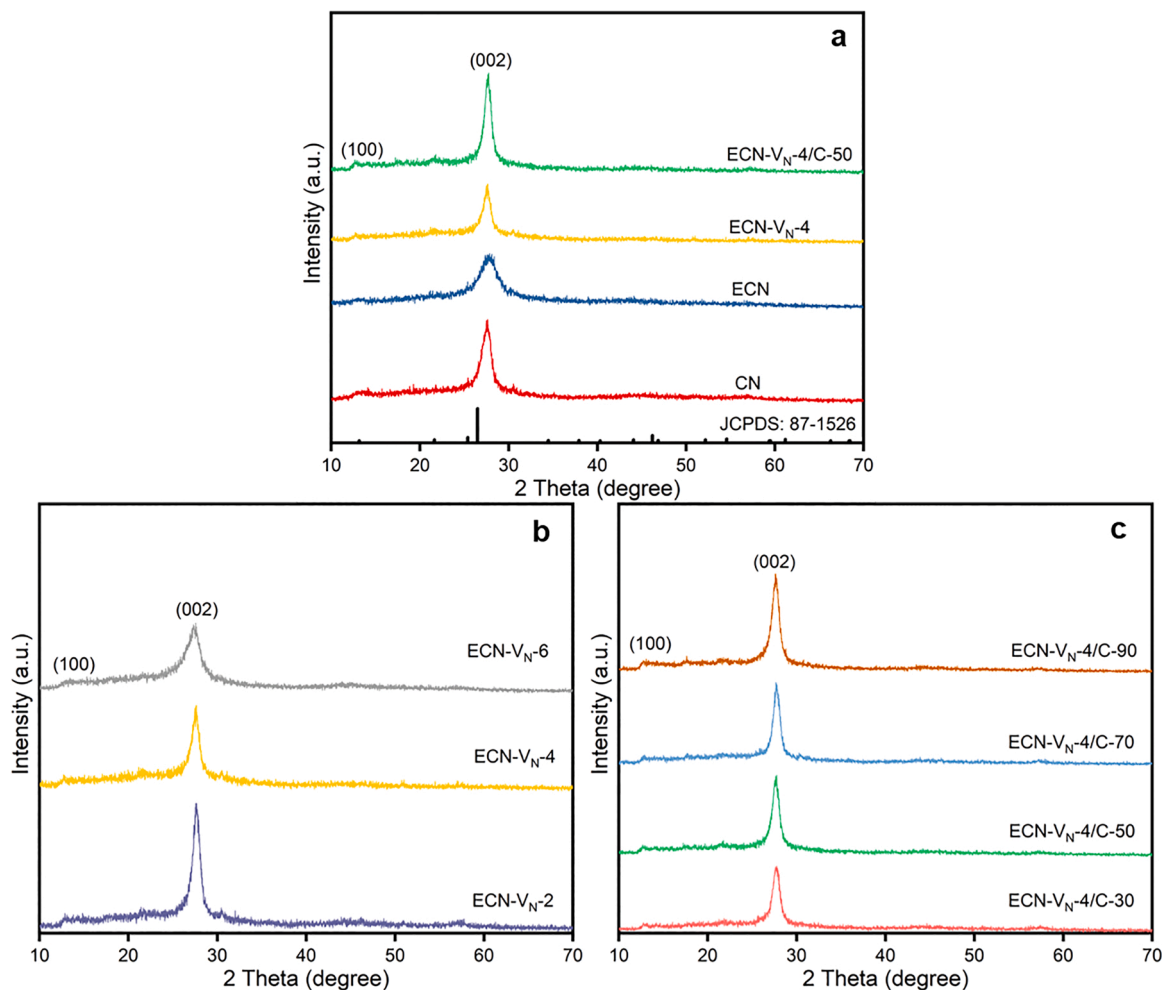


Fig. 1. XRD patterns of (a) CN, ECN, ECN-VN-4, and ECN-VN-4/C-50; (b) ECN-VN-2, ECN-VN-4, ECN-VN-6; and (c) ECN-VN-4/C-30, ECN-VN-4/C-50, ECN-VN-4/C-70, and ECN-VN-4/C-90.

JEOL, JEM-2100 F), and atomic force microscope (AFM, Oxford Instruments, Cypher S) were used to characterize the crystal structures, morphology, fine structures, and surface topography of the photocatalysts, respectively. Their light absorption properties and band gaps were determined with UV-Vis diffuse reflectance spectroscopy (DRS) (Shimadzu, UV3600 PLUS). Fourier transform infrared spectroscopy (FTIR, Thermo Fisher, Nicolet iS50), Raman spectra (HORIBA, LabRAM Aramis), and X-ray photoelectron spectroscopy (XPS, Kratos Analytical, AXIS Supra) were used to obtain further information on chemical compositions of the photocatalysts. The Brunauer-Emmett-Teller (BET) surface areas and pore volumes of the prepared samples were measured on an accelerated surface area and porosimetry system (Micromeritics, ASAP 2020 plus).

The separation efficiency of photo-induced carriers in the photocatalysts was characterized with photoluminescence (PL) spectroscopy (Edinburgh, FLS980), photocurrent response (Chenhua, CHI760E), and electrochemical impedance spectroscopy (EIS, Chenhua, CHI760E). The dynamic behavior of photogenerated carriers in the photocatalyst was investigated by steady-state surface photovoltage (SPV) spectroscopy (CEAULIGHT, CEL-SPS1000). Electron paramagnetic resonance spectra (EPR, Bruker, EXXplus-6/1) were obtained to verify the presence of nitrogen vacancies in the photocatalysts.

### 2.3. Photocatalytic hydrogen production

Photocatalytic hydrogen production by water splitting was evaluated

using an on-line photocatalytic hydrogen production system (Beijing Perfectlight, Labsolar-6A). Simulated sunlight was produced by a 300 W Xenon lamp with an AM 1.5 G filter. The prepared photocatalyst (50 mg) was uniformly dispersed into 50 mL aqueous solution containing 10 vol% triethanolamine (TEOA, as a hole sacrificial agent) and 2.0 wt% Pt (in the form of  $H_2PtCl_6$ , as a co-catalyst) in the photocatalytic reactor, which was maintained at 5 °C by a refrigerated circulating bath. The photocatalytic system and the reactor were completely vacuumized for 30 min prior to the start of simulated sunlight illumination to ensure complete removal of air. The hydrogen produced was analyzed by an online gas chromatograph (Techcomp, GC-910) equipped with a thermal conductivity detector, and argon was used as the carrier gas. To evaluate the hydrogen production from photocatalytic decomposition of TEOA, photocatalytic hydrogen production experiments were conducted following the same procedures of photocatalytic water splitting, except that 50 mL TEOA containing 2.0 wt% Pt (in the form of  $H_2PtCl_6$ ), instead of 50 mL aqueous solution containing 10 vol% TEOA and 2.0 wt% Pt, was used.

The photocatalyst's apparent quantum efficiency (AQE) for hydrogen production (at 420 nm) was calculated as [37]:

$$AQE (\%) = \frac{2N_{H_2}}{N_{photons}} \times 100 \quad (1)$$

where  $N_{H_2}$  and  $N_{photons}$  are the number of hydrogen molecules produced and the number of incident photons in the photocatalytic system, respectively.



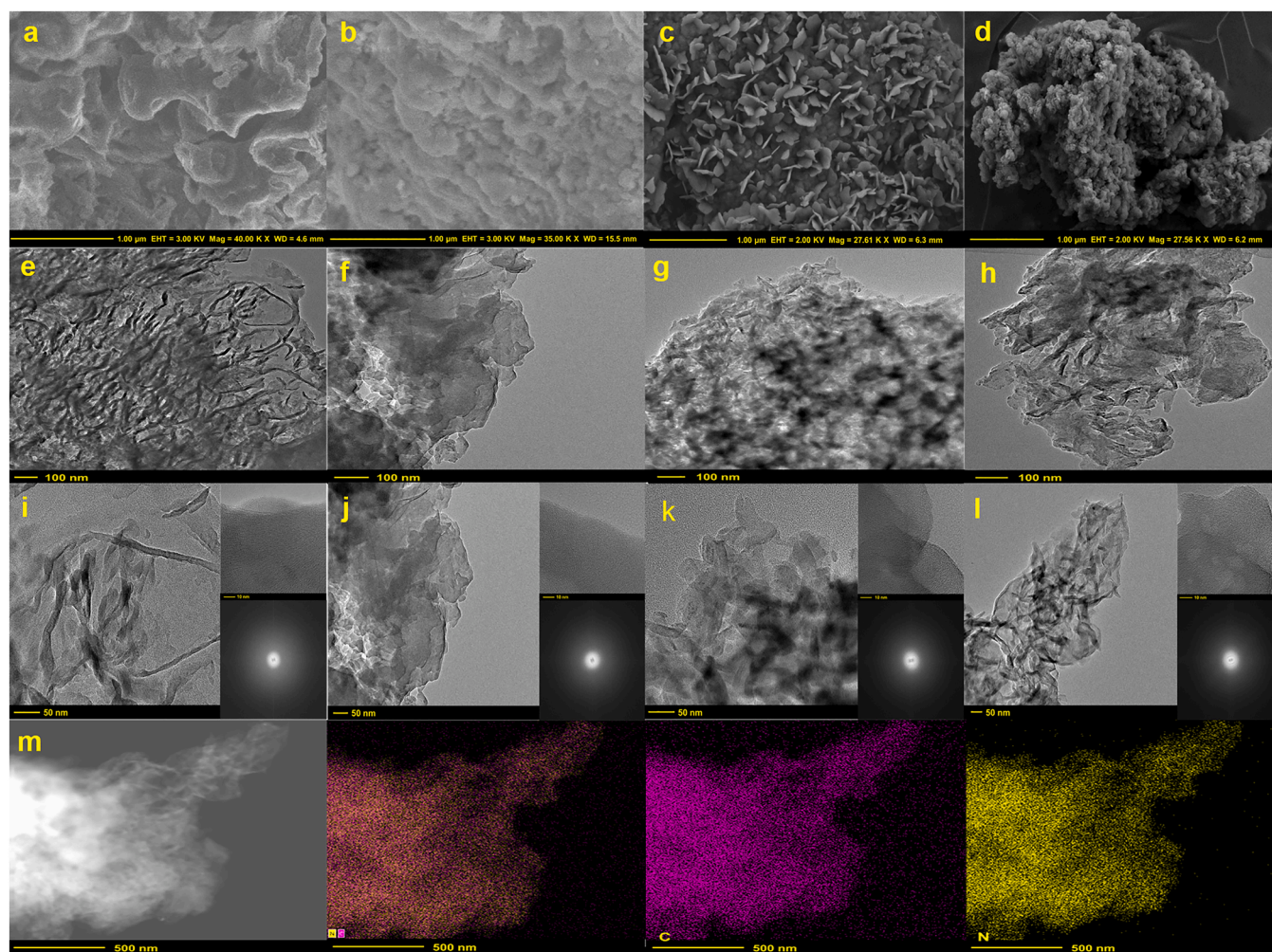


Fig. 2. SEM micrographs of (a) CN, (b) ECN, (c) ECN-VN-4, and (d) ECN-VN-4/C-50; TEM micrographs of (e) CN, (f) ECN, (g) ECN-VN-4, and (h) ECN-VN-4/C-50; amplified TEM images of (i) CN, (j) ECN, (k) ECN-VN-4, and (l) ECN-VN-4/C-50; and elemental mapping of ECN-VN-4/C-50 (m).

## 2.4. DFT calculations

DFT calculations were performed with employment of the ultrasoft pseudopotentials to model the interaction between the ion core and the valence electrons. The generalized-gradient-approximation (GGA) of Perdew-Burke-Ernzerhof (PBE) functional was used to form the exchange correlation function. In all calculations, the kinetic cut-off energy was set at 350 eV and a  $6 \times 6 \times 6$  K-points mesh was employed for structure optimization. Under the above settings, the convergence tolerance of energy, maximum force, maximum displacement, and self-consistent field (SCF) tolerance were determined to be  $1.0 \times 10^{-5}$  eV/atom, 0.03 eV/Å, 0.01 Å, and  $1.0 \times 10^{-6}$  eV/atom, respectively. After geometry optimization, the energy band structure and density of state (DOS) of CN, CN-VN, and CN-VN/C were calculated. To calculate the work functions ( $W_f$ ) of different components and avoid the interaction between repeated slabs, a uniform vacuum width of 15 Å was adopted, and the K-points were set to  $5 \times 5 \times 1$ .  $W_f$  was determined as the energy difference between the vacuum level ( $E_v$ ) and the Fermi energy ( $E_f$ ) [38]:

$$W_f = E_v - E_f \quad (2)$$

## 3. Results and discussion

### 3.1. Characterization of the prepared photocatalysts

The crystal structures of the prepared photocatalysts were

investigated by XRD. On Fig. 1, the peaks at  $2\theta$  values of  $13.0^\circ$  and  $27.6^\circ$  were attributed to the (100) and (002) crystal planes of CN [39], which arise from the interplanar packing of s-triazine ring units and the interlayer stacking of aromatic segments, respectively [40]. Fig. 1a indicates that the intensity of (002) diffraction peak associated with the interlayer stacking was obviously weakened after the exfoliation of CN, demonstrating that the multilayered CN was successfully exfoliated [34]. After 4 h of calcination (ECN-VN-4), the diffraction peak of (002) crystal plane narrowed down a little bit compared with ECN. As the calcination time was increased from 2 to 6 h, the intensity of (002) diffraction peak became weaker while its width became broader (Fig. 1b). Such changes were attributed to the destruction of long-range order in atomic arrangements with the formation of nitrogen vacancies brought by progressive calcination [35]. The (002) diffraction peak shifted slightly towards lower  $2\theta$  values with increasing dosage of HMTA (Fig. 1c), suggesting that the interlayer stacking distance increased as a result of the intercalation of more carbon species in the interlayer region of ECN-VN-4 [41].

Fig. 2 shows the SEM and TEM micrographs of CN, ECN, ECN-VN-4, and ECN-VN-4/C-50. While CN and ECN occurred as folded nanosheets (Fig. 2a and b), flake-like morphology dominated after 4 h of calcination due to the formation of nitrogen vacancies (Fig. 2c). A three-dimensional honeycomb structure composed of small flakes were formed after intercalation of carbon species (Fig. 2d). The structural hierarchy of the prepared photocatalysts is shown more clearly on the TEM micrographs. While CN had a multilayered structure (Fig. 2e), ECN particles were



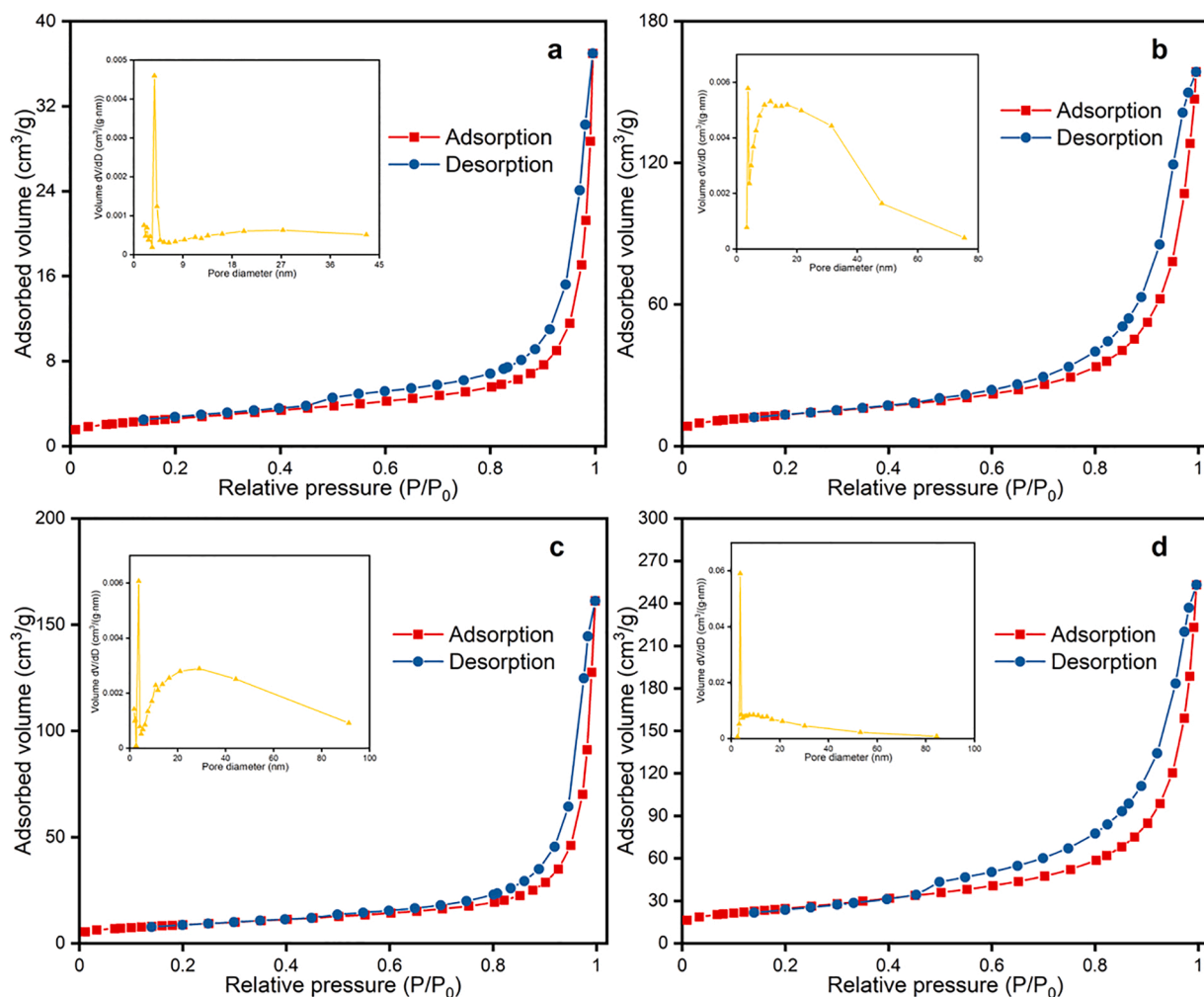


**Fig. 3.** Nitrogen adsorption-desorption isotherms and pore size distribution of (a) CN, (b) ECN, (c) ECN-VN-4, and (d) ECN-VN-4/C-50. The pore size distribution was calculated from the desorption branch of isotherm by the Barrett-Joyner-Halenda (BJH) method.

much thinner and were composed of much less number of layers (Fig. 2f). ECN-VN-4 was composed of small ultra-thin nanosheets (Fig. 2g), while the nanosheets of ECN-VN-4/C-50 appeared to be even thinner (Fig. 2h). None of these photocatalysts showed lattice fringes, and fast Fourier transform (FFT) patterns further proved that their structures were all amorphous (Fig. 2i-l). Based on the structural details revealed by SEM and TEM, ECN-VN-4/C-50, with a three-dimensional honeycomb structure, probably has more exposed surface compared to the multilayered CN, thin-layered ECN, and small nanosheet-like ECN-VN-4. The larger specific surface area of ECN-VN-4/C-50 (as confirmed by BET surface area measurements later) would allow more active sites to contact surface molecules, which translates into higher photocatalytic activity. The surface topography of CN, ECN, ECN-VN-4, and ECN-VN-4/C-50 was characterized with AFM. As shown on Fig. S1, the thicknesses of CN and ECN were about 5.8 and 1.2 nm, respectively, which supports that the multilayered CN was successfully exfoliated into thin nanosheets. After the formation of nitrogen vacancies and intercalation of carbon species, the thickness of the nanosheets increased slightly to around 1.6 and 1.8 nm, respectively. The energy-dispersive X-ray (EDX) mapping of CN, ECN-VN-4, and ECN-VN-4/C-50 showed homogeneous distribution of carbon and nitrogen elements (Fig. S2a, b and Fig. 2m), confirming their elemental compositions.

Fig. 3 shows the nitrogen adsorption-desorption isotherms and calculated pore size distribution of the photocatalysts. The BET surface areas of CN, ECN, ECN-VN-4, and ECN-VN-4/C-50 were determined to be 9.25, 47.31, 31.31, and 86.53 m²/g, respectively. As expected,

exfoliation of the multilayered CN resulted in drastic increase in the specific surface area (by more than five times), while the BET surface area of ECN decreased significantly with formation of nitrogen vacancies after calcination. Specifically, the BET surface areas of ECN-VN-2, ECN-VN-4, and ECN-VN-6 were 33.46, 31.31, and 27.05 m²/g, respectively (Fig. S3a, Fig. 3c, and Fig. S3b). After intercalation of carbon species, the BET surface area of ECN-VN-4/C-50 was significantly increased (to 86.53 m²/g), which is attributed to the formation of a folded honeycomb structure. The pore sizes of CN lied primarily between 2 and 5 nm, while those of ECN were spread in the range of 2–75 nm, which further proves that the multilayered CN was exfoliated into thin nanosheets. The pore sizes were further enlarged (2–90 nm) after introduction of nitrogen vacancies. Overall, the BET surface area of ECN decreased while its pore size increased with the formation of vacancies through calcination, and the effect was more prominent for the ECN treated with longer calcination times. This resulted from the disappearance of some small pores and formation of larger pores from the collapse of CN skeleton (i.e., structural deformation) brought by the creation of more nitrogen vacancies. As shown on Fig. S3a, Fig. 3c, and Fig. S3b, more nitrogen atoms were lost from ECN, while the skeleton collapsed more significantly and the sizes of the mesopores were enlarged gradually with increases in the calcination time. Due to the embedding of carbon species and formation of the three-dimensional honeycomb structure, the pore sizes of ECN-VN-4/C-50 were reduced to the range of 2–5 nm. As greater specific surface areas can generally provide more surface active sites [42], ECN-VN-4/C-50 is expected to

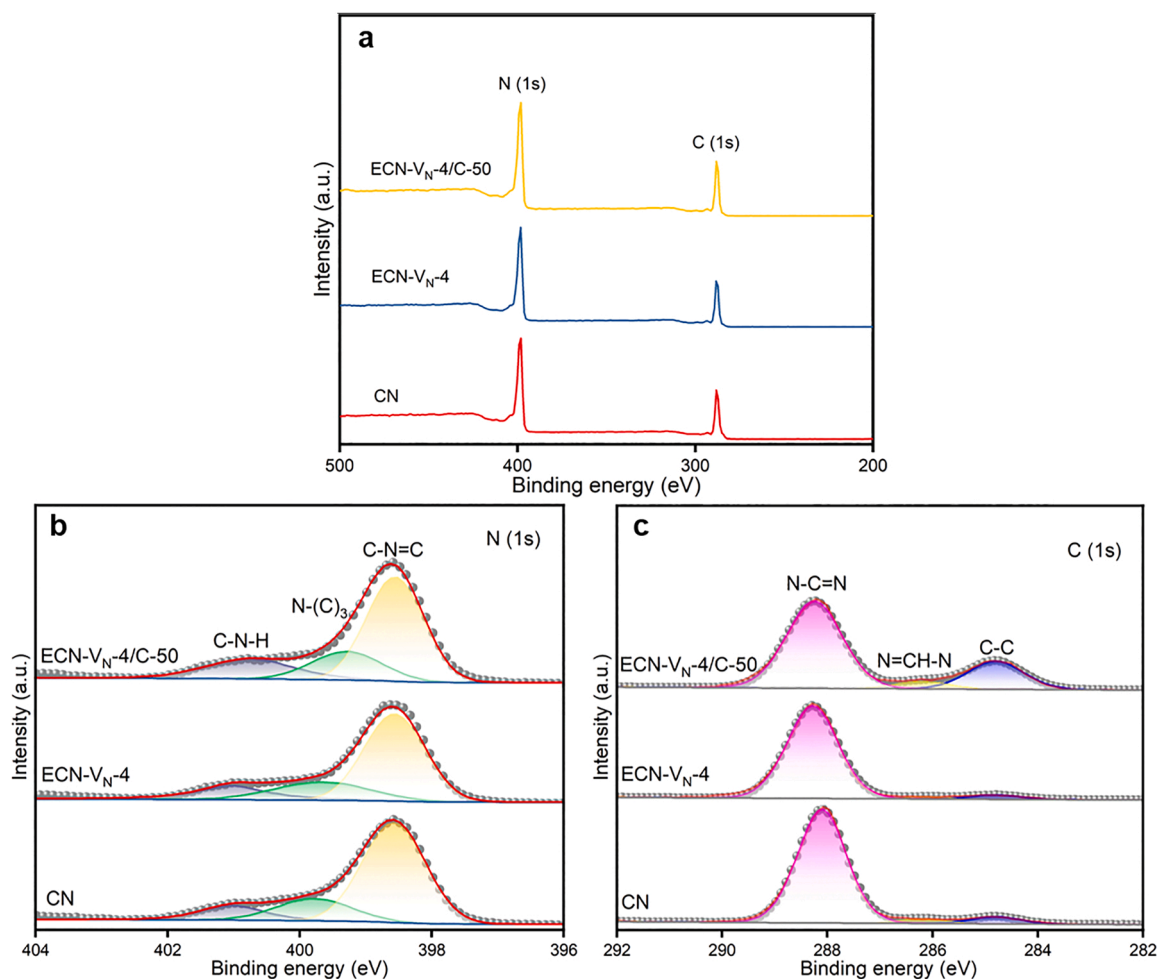


Fig. 4. XPS spectra of CN, ECN-VN-4, and ECN-VN-4/C-50: (a) survey, (b) N (1 s), and (c) C (1 s).

have higher photocatalytic activity than CN, ECN, and ECN-VN-4.

The nitrogen vacancies and intercalated carbon species on the photocatalysts were investigated with XPS. The survey spectra of CN, ECN-VN-4, and ECN-VN-4/C-50 displayed strong signals of C and N (Fig. 4a). The peaks located at 401.5, 399.8, and 398.6 eV were assigned to C-N-H, N-(C)<sub>3</sub>, and C-N=C, respectively (Fig. 4b) [43]. It is worth noting that the peak-area ratio between C-N=C and N-(C)<sub>3</sub> decreased from 3.80 in CN to 3.02 in ECN-VN-4, supporting the preferential loss of nitrogen atoms at the C-N=C site [35]. To further verify the loss site of nitrogen atoms, XPS spectra for ECN-VN-2, ECN-VN-4, and ECN-VN-6 were also collected (Fig. S4b). The peak-area ratios between C-N=C and N-(C)<sub>3</sub> were 3.41, 3.02, and 2.65 for ECN-VN-2, ECN-VN-4, and ECN-VN-6, respectively, which further confirms that the nitrogen atoms at the C-N=C site were preferentially lost during the calcination process. The peak-area ratio between C-N=C and N-(C)<sub>3</sub> in ECN-VN-4/C-50 barely changed after the intercalation of carbon species, indicating that the introduced carbon species did not form C-N=C or N-(C)<sub>3</sub>. The C (1 s) peaks at 288.1, 286.2 and 284.8 eV were attributed to N-C=N, N=CH-N, and C-C/C=C, respectively (Fig. 4c) [44]. Compared with those of CN and ECN-VN-4, C-C/C=C peaks clearly appeared on the XPS spectrum of ECN-VN-4/C-50. Based on the preparation procedure of ECN-VN-4/C-50, the C-C/C=C signals arose from the carbon species formed from the sublimation of HMTA. The peak position of the C-C/C=C in ECN-VN-4/C-50 is consistent with that of graphitic carbon reported in the literature [45]. Therefore, it could be inferred that the typical sp<sup>2</sup> hybrid C-C/C=C bond in the intercalated carbon species existed in the form of graphitic carbon structure [41].

Fig. 5a displays the UV-Vis DRS spectra of the prepared

photocatalysts. The absorption edge of ECN showed a slight blue shift compared with that of CN, and the band gap increased from 2.75 to 2.98 eV (Fig. 5b). This can be attributed to the reduction of conjugation length and the effect of strong quantum confinement caused by the exfoliated CN nanosheets [34]. Compared with ECN, the light absorption edge of ECN-VN-4 shifted to the longer wavelength range, and it had a narrower band gap of 2.13 eV (Fig. 5b). These results suggest that formation of nitrogen vacancies effectively reduces the band gap and improves the light absorption of ECN. Fig. S5a and b further show that the light absorption of ECN also increased with the formation of more nitrogen vacancies. The enhancement in light absorption probably results from the increased p-electron delocalization in the conjugated system [35]. The absorption band of ECN-VN-4/C-50 displayed a slight red shift (Fig. 5a), suggesting that intercalation of carbon species also affected the light absorption of ECN-VN [36].

Fig. 5c shows the FTIR spectra of the prepared photocatalysts. The broad absorption peak between 3000 and 3400 cm<sup>-1</sup> was attributed to the N-H stretching vibration and the O-H stretching band [46]. The peaks at 1638 and 1553 cm<sup>-1</sup> corresponded to sp<sup>2</sup> C=N stretching vibrations [47,48], while those at 1403, 1319, and 1230 cm<sup>-1</sup> were ascribed to the aromatic sp<sup>3</sup> C-N stretching [48]. The intense peak at around 807 cm<sup>-1</sup> belonged to the out-of-plane skeletal bending of triazine ring [49]. After being exfoliated (ECN), the structure of CN was not destroyed, while the intensity of these characteristic peaks decreased slightly with the formation of nitrogen vacancies (ECN-VN-4). The intensity of all absorption peaks of ECN-VN decreased as the calcination time increased (Fig. S5c), which is attributed to the cleavage of chemical bonds with the progressive loss of nitrogen atoms during the calcination

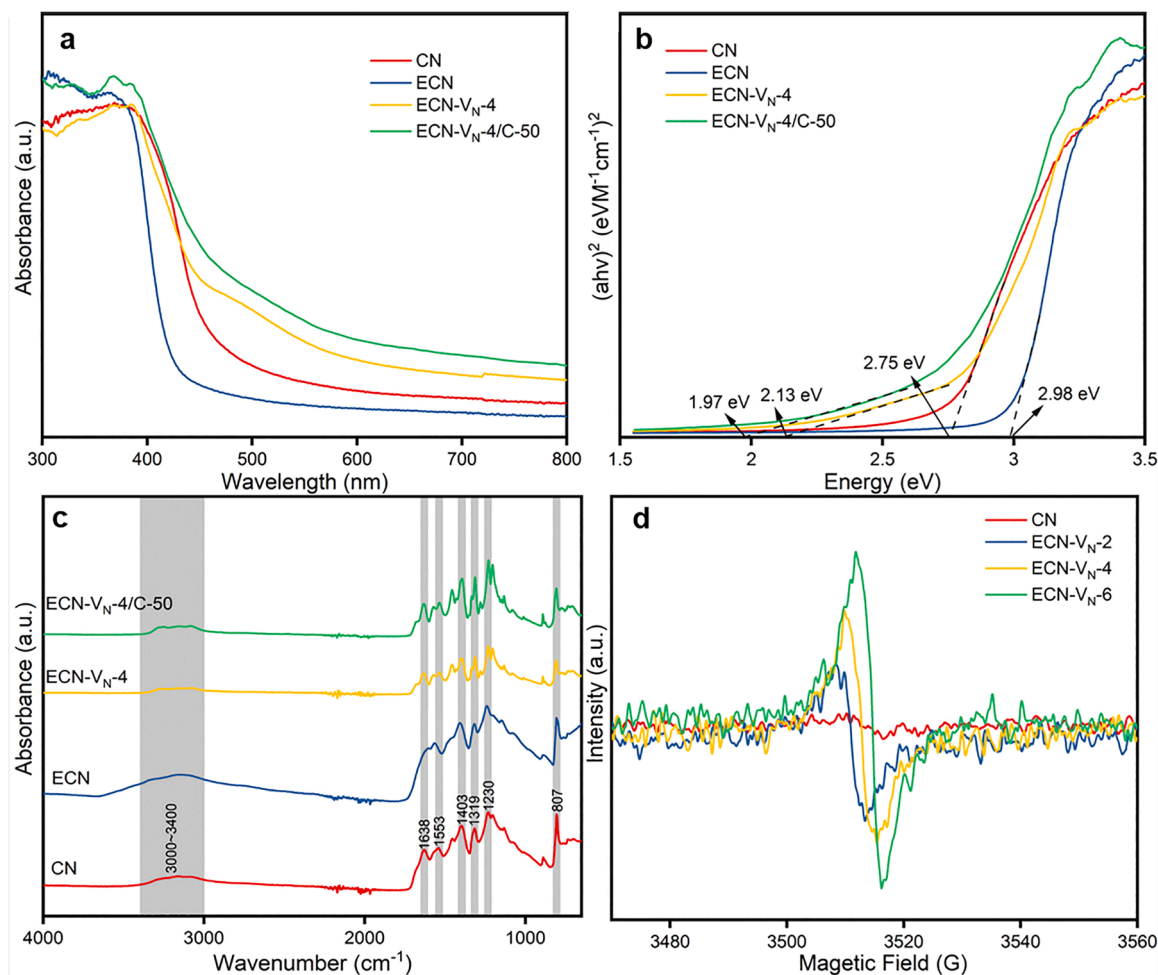


**Fig. 5.** UV-Vis DRS spectra (a) and determination of the band gaps (b), and FTIR spectra (c) of CN, ECN, ECN-V<sub>N</sub>-4, and ECN-V<sub>N</sub>-4/C-50; and EPR spectra (d) of CN, ECN-V<sub>N</sub>-2, ECN-V<sub>N</sub>-4, and ECN-V<sub>N</sub>-6.

process [35]. The FTIR spectra showed no apparent change after intercalation of carbon species (ECN-V<sub>N</sub>-4/C-50), and increases in the content of carbon species made little difference (Fig. S5d), indicating that the HMTA treatment did not change the structure of ECN-V<sub>N</sub> [36]. The FTIR spectra of CN, ECN, ECN-V<sub>N</sub>-4, and ECN-V<sub>N</sub>-4/C-50 indicate that these photocatalysts had essentially identical structural composition. To further verify this, Raman spectra, which are complementary to FTIR spectra, of these photocatalysts were also obtained (Fig. S5e). The Raman spectra of CN, ECN, ECN-V<sub>N</sub>-4, and ECN-V<sub>N</sub>-4/C-50 were found to be quite similar, further confirming that the structural composition of these photocatalysts was almost the same. Together, both FTIR and Raman characterization results consistently show that the skeleton structure of CN was barely changed with exfoliation, formation of nitrogen vacancies, and intercalation of carbon species.

To further prove the existence of nitrogen vacancies, EPR spectra of CN, ECN-V<sub>N</sub>-2, ECN-V<sub>N</sub>-4, and ECN-V<sub>N</sub>-6 were collected (Fig. 5d). While no paramagnetic absorption was observed for CN, ECN-V<sub>N</sub>-2, ECN-V<sub>N</sub>-4, and ECN-V<sub>N</sub>-6 exhibited obvious absorption signal, whose intensity increased with the calcination time of ECN-V<sub>N</sub>. The paramagnetic absorption signals of ECN-V<sub>N</sub> can be attributed to the unpaired electrons on carbon atoms of the  $\pi$ -conjugated aromatic rings [35]. The introduction of nitrogen vacancies can reassign the extra electrons to neighboring carbon atoms through the delocalized  $\pi$ -conjugated networks of CN [50]. The more enhanced EPR signal of ECN-V<sub>N</sub> with longer calcination time indicates that the number of nitrogen vacancies increased with the duration of calcination treatment [51].

PL, photocurrent response, and EIS spectra were used to

quantitatively evaluate the separation and transfer of photogenerated charge carriers in the photocatalysts. Fig. 6a shows the PL spectra of CN, ECN-V<sub>N</sub>-4, and ECN-V<sub>N</sub>-4/C-50 under light excitation at 365 nm. The fluorescence intensity of ECN-V<sub>N</sub>-4 was much lower than that of CN, which indicates that the presence of nitrogen vacancies effectively inhibited the recombination of photogenerated carriers. ECN-V<sub>N</sub>-4 also exhibited lower fluorescence intensity compared to ECN-V<sub>N</sub>-2 and ECN-V<sub>N</sub>-6 (Fig. S6). Increasing the number of nitrogen vacancies is favorable for inhibiting the recombination of photogenerated carriers, but too many nitrogen vacancies could be counter-productive by serving as the recombination centers for photogenerated carriers. The presence of excessive nitrogen vacancies could lead to narrowing of the band gap and reduction in the redox capacity of carriers, and thus increase the chance for the recombination of photogenerated carriers. ECN-V<sub>N</sub>-4 was observed to have the lowest PL fluorescence intensity, suggesting the level of nitrogen vacancies on ECN was optimum after being calcinated (at 620 °C) for 4 h. The PL intensity of ECN-V<sub>N</sub>-4/C-50 was even lower than that of ECN-V<sub>N</sub>-4 (Fig. 6a), suggesting that intercalation of carbon species greatly enhanced the separation of photogenerated carriers. Thus, ECN-V<sub>N</sub>-4/C-50 is expected to have the highest photocatalytic activity among the photocatalysts prepared.

The charge carrier dynamics of the prepared photocatalysts was investigated by time-resolved photoluminescence spectroscopy (Fig. 6b). The PL decay curves were fitted by the following equation [52]:

$$I(t) = A_1 \exp(-t/\tau_1) + A_2 \exp(-t/\tau_2) \quad (3)$$



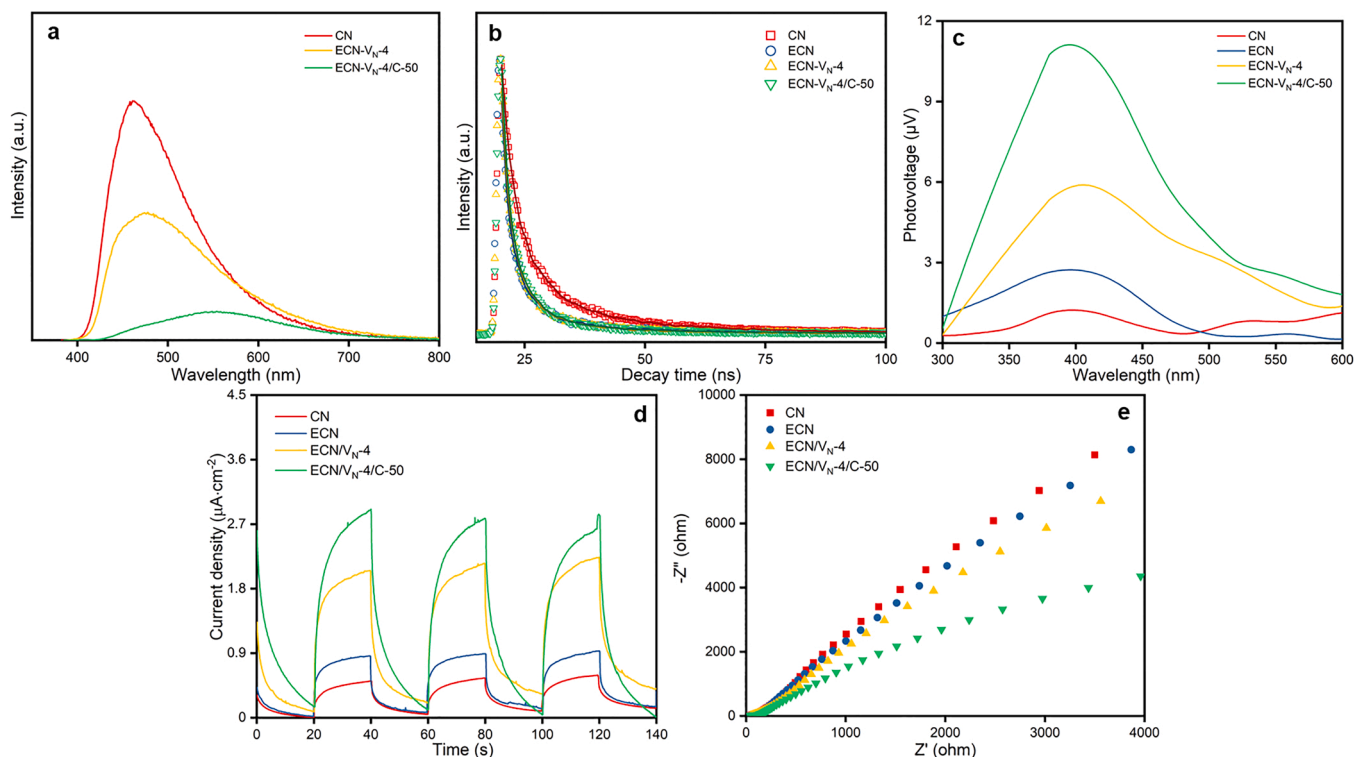


**Fig. 6.** Characterization of the separation efficiency of photogenerated carriers in CN, ECN, ECN-VN-4, and ECN-VN-4/C-50: (a) PL spectra, (b) time-resolved photoluminescence spectra, (c) SPV spectra, (d) photocurrent response spectra, and (e) Nyquist plot of EIS spectra.

where  $\tau_1$  and  $\tau_2$  are the corresponding fluorescence lifetimes, and  $A_1$  and  $A_2$  are the amplitudes of the corresponding components. The radiative recombination lifetime ( $\tau$ ) of the photocatalyst was then estimated as [52]:

$$\tau = \frac{A_1 \tau_1^2 + A_2 \tau_2^2}{A_1 \tau_1 + A_2 \tau_2} \quad (4)$$

The calculated radiative recombination lifetimes of the CN, ECN, ECN-VN-4, and ECN-VN-4/C-50 were 17.21, 14.77, 12.13, and 11.48 ns, respectively. ECN had a lower radiative recombination lifetime than CN, which resulted from the fact that the few-layered ECN had shortened carrier migration distance and thus reduced recombination of photogenerated carriers during the migration process. After the introduction of nitrogen vacancies (ECN-VN-4), the radiative recombination lifetime was further lowered, which could be attributed to the transfer of electrons or holes to some favorable defect states. ECN-VN-4/C-50 showed the lowest radiative recombination lifetime, because its larger specific surface area provided more active sites for surface reactions, and carbon-rich induction also enhanced its conductivity and accelerated the migration rate of photogenerated carriers, which facilitated the capture of photogenerated electrons by the active sites.

The SPV spectra of CN, ECN, ECN-VN-4, and ECN-VN-4/C-50 all showed positive signals (Fig. 6c), which are typical of n-type semiconductors [53], and are indicative of migration of positive charges from the inside of photocatalysts to the surface. Among the four photocatalysts evaluated, ECN-VN-4/C-50 showed the strongest SPV signal, confirming that it has the strongest separation efficiency of photogenerated carriers. Fig. 6d shows that CN, ECN-VN-4, and ECN-VN-4/C-50 all exhibited fast and uniform photocurrent response under simulated sunlight illumination. Among the three photocatalysts, ECN-VN-4/C-50 had the highest photocurrent response, which is indicative of much better separation of photogenerated carriers. Fig. S7a shows that ECN-VN-4 had a higher photocurrent response than ECN-VN-2 and ECN-VN-6, which confirms that the level of nitrogen

vacancies on ECN was optimum after being calcinated (at 620 °C) for 4h. Fig. S7b indicates that ECN-VN-4/C-50 exhibited a higher photocurrent response than the ECN-VN-4 photocatalysts intercalated with carbon species at other levels. These results further suggest that intercalation with proper amount of carbon species can greatly enhance the photocatalytic activity of ECN-VN-4. Fig. 6e shows that the arc radius of ECN-VN-4/C-50 was much smaller than those of CN and ECN-VN-4, suggesting that ECN-VN-4/C-50 has better electron conductivity and mobility. The Nyquist plot of EIS spectra (Fig. S7c) indicate that the arc radius decreased with increases in nitrogen vacancies on ECN-VN photocatalysts, which could be attributed to the increased  $\pi$ -electron delocalization brought by greater loss of nitrogen atoms [35]. Meanwhile, the conductivity of the ECN-VN-4 photocatalysts increased gradually with the amount of carbon species intercalated (Fig. S7d). Together, the PL, SPV, photocurrent response, and EIS results consistently indicate that ECN-VN-4/C-50 has more efficient separation and migration of photogenerated carriers than CN, ECN-VN-4, which is attributed to the synergy of nitrogen vacancies and intercalation of carbon species.

### 3.2. Photocatalytic hydrogen production

Fig. 7a compares the photocatalytic hydrogen production performance of CN, ECN, ECN-VN-4, and ECN-VN-4/C-50 under the illumination of simulated sunlight. Hydrogen production almost increased linearly with illumination time in the presence of all four photocatalysts. The amount of hydrogen generated from water splitting reached 1208.4, 2484.8, 5303.6, and 14,582.1  $\mu\text{mol/g}$ , in the presence of CN, ECN, ECN-VN-4, and ECN-VN-4/C-50, respectively, after 180 min of illumination. The calculated AQE values of CN, ECN, ECN-VN-4, and ECN-VN-4/C-50 for photocatalytic hydrogen production (at 420 nm) were 0.62%, 1.15%, 2.33%, and 6.98%, respectively. The higher photocatalytic activity of ECN compared to CN is attributed to the reduced electron migration distance after exfoliation of the multilayered CN into thin nanosheets, which reduces the recombination of photogenerated carriers. In addition, the increase in specific surface area also provides more

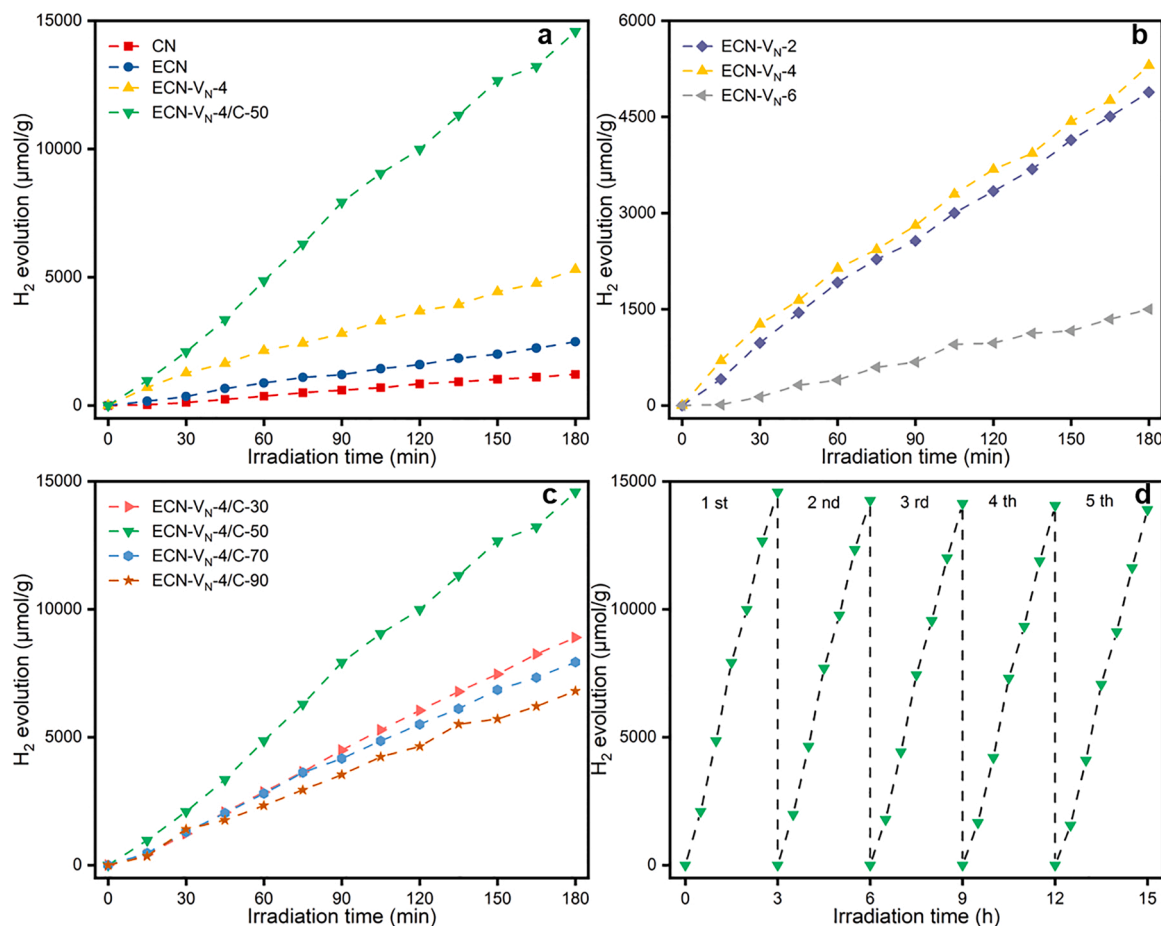


**Fig. 7.** Photocatalytic hydrogen production under simulated sunlight illumination: (a) photocatalytic activity of CN, ECN, ECN-VN-4, and ECN-VN-4/C-50; (b) effect of nitrogen vacancies; (c) effect of HMTA dose; and (d) performance of ECN-VN-4/C-50 over five consecutive cycles of use.

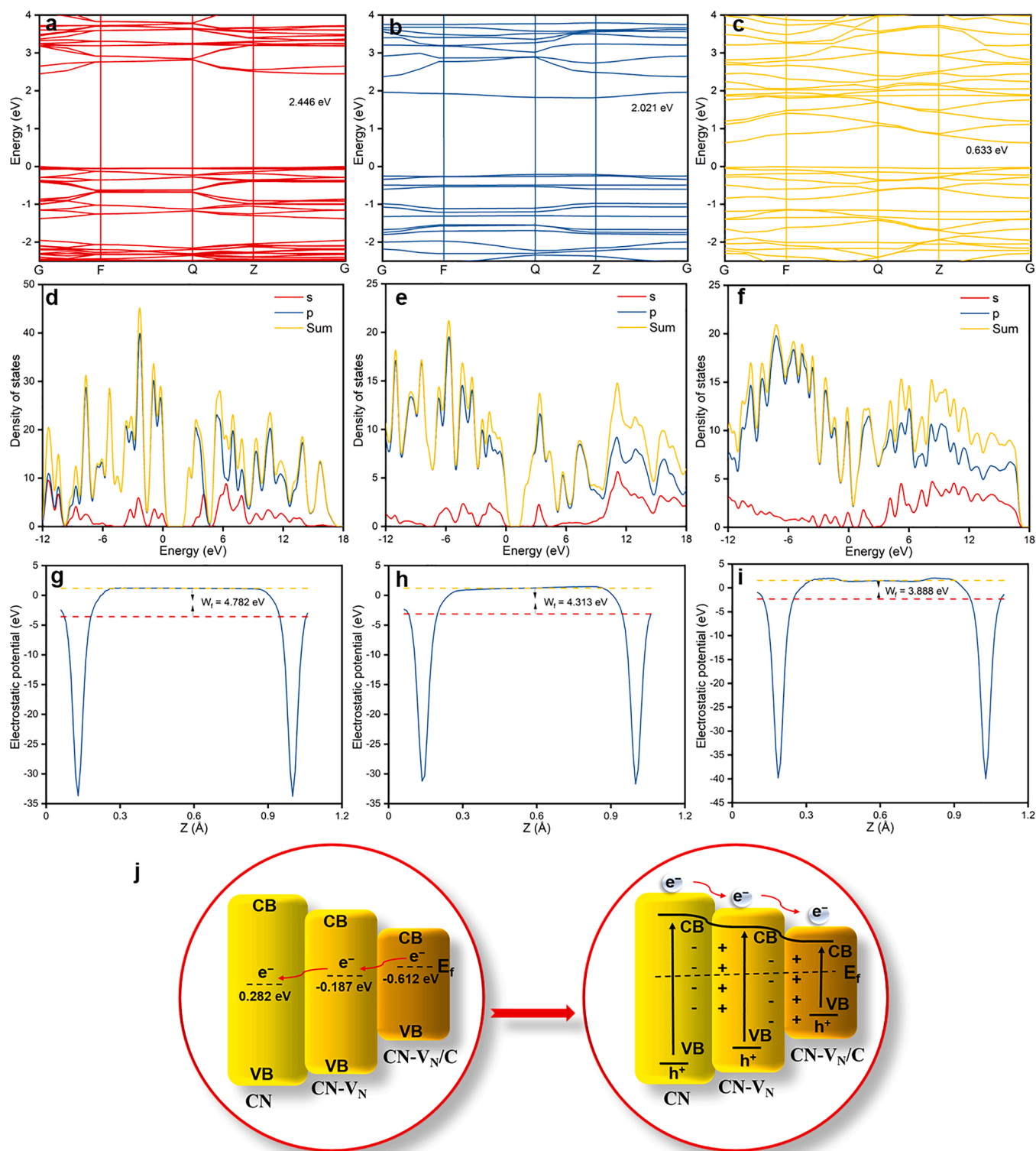
reactive sites, which can improve photocatalytic activity. The photocatalytic activity further increased with the formation of nitrogen vacancies. The defects from loss of nitrogen atoms create additional energy levels in the intrinsic band gap of ECN, thereby broadening the light absorption range, and more photogenerated carriers are produced from receiving more light energy. At the same time, the introduction of nitrogen vacancies as electron or hole traps also helps to suppress the recombination of photogenerated electron-hole pairs and optimize the original  $\pi$ -conjugated system of ECN. This triggers the redistribution of charges, which significantly promotes the participation of electrons in photocatalytic reactions. Among the photocatalysts prepared, ECN-VN-4/C-50 exhibited the highest photocatalytic activity. This unique carbon-rich three-dimensional nanostructure provides a large number of active sites for photocatalytic reactions, has increased absorption of visible light, and possesses a multi-directional photogenerated charge transfer pathway, which greatly enhance the separation of the photogenerated carriers and surface reaction rates. In addition, dual BIEFs can be formed within ECN-VN-4/C-50 due to the synergy of nitrogen vacancies and intercalation of carbon species, which can effectively separate the photogenerated carriers (to be discussed later).

Fig. 7b compares the photocatalytic hydrogen production of ECN-VN with different calcination times (2, 4, and 6 h). After 2 h of calcination, photocatalytic hydrogen production increased from 2484.8 μmol/g (ECN) to 4887.9 μmol/g (ECN-VN-2) by 180 min of simulated sunlight illumination. The enhanced photocatalytic activity can be attributed to the combined effect of improved light absorption and more efficient separation of photogenerated carriers with the introduction of nitrogen vacancies. The photocatalytic hydrogen production was further increased to 5303.6 μmol/g (ECN-VN-4) when the calcination time of

ECN was increased to 4 h. However, the hydrogen production dropped to 1499.7 μmol/g (ECN-VN-6) after 6 h of calcination. Such significant compromise in photocatalytic performance is attributed to the increased recombination of photogenerated carriers brought by the over-introduction of nitrogen vacancies [54].

Fig. 7c depicts the effect of HMTA dose on the hydrogen production activity of ECN-VN/C photocatalyst. The amount of hydrogen produced reached 8901.0, 14,582.1, 7934.8, and 6801.6 μmol/g in the presence of ECN-VN-4/C-30, ECN-VN-4/C-50, ECN-VN-4/C-70, and ECN-VN-4/C-90, respectively, after 180 min of simulated sunlight illumination. The activity of the photocatalysts apparently followed the volcano-shaped curve with respect to the amount of intercalated carbon species. While intercalation of proper amount of carbon species augments the photocatalyst's light absorption, optimizes its energy band structure, and strengthens the delocalized  $\pi$  bond, the presence of excessive amount of carbon species could compromise its photocatalytic activity as they also serve as the trapping sites for electrons or holes and promote the recombination of electron-hole pairs [36].

To determine the source of hydrogen produced in photocatalytic water splitting, photocatalytic decomposition of TEOA (containing 2.0 wt% Pt as a co-catalyst) was also investigated. Almost no hydrogen was produced in the absence of photocatalyst, while the hydrogen yields were 50.6, 66.3, 121.9, and 334.2 μmol/g in the presence of CN, ECN, ECN-VN-4, and ECN-VN-4/C-50, respectively, after 180 min of simulated sunlight illumination (Fig. S8a). In contrast, the yields of hydrogen from water splitting, which was conducted with aqueous solution containing 10% TEOA and 2.0 wt% Pt, were 1208.4, 2484.8, 5303.6, and 14,582.1 μmol/g, in the presence of CN, ECN, ECN-VN-4, and ECN-VN-4/C-50, respectively, under the same conditions. Compared to



**Fig. 8.** Energy-band structures for (a) CN, (b) CN-V<sub>N</sub>, and (c) CN-V<sub>N</sub>/C; total DOS for (d) CN, (e) CN-V<sub>N</sub>, and (f) CN-V<sub>N</sub>/C; calculated electrostatic potential of (g) CN, (h) CN-V<sub>N</sub>, and (i) CN-V<sub>N</sub>/C; and (j) band structures of CN-V<sub>N</sub>/C before and after the alignment of the Fermi levels.

photocatalytic decomposition of TEOA, the hydrogen yields in the presence of the same photocatalysts were 23.9–43.5 times higher when 10% of TEOA was used as a hole sacrificial agent in water. Thus, no more than 0.5% of the hydrogen produced in photocatalytic water splitting could come from the decomposition of TEOA. Instead, TEOA served as an efficient sacrificial agent and consumed holes to reserve a large number of electrons for the reduction of protons to hydrogen in the

photocatalytic system.

To verify the role of Pt as a co-catalyst in the photocatalytic system, photocatalytic hydrogen production experiments were also conducted in the absence of it. The hydrogen yields from water splitting were only 50.9, 94.6, 189.0, and 373.9  $\mu\text{mol/g}$ , in the presence of CN, ECN, ECN-V<sub>N</sub>-4, and ECN-V<sub>N</sub>-4/C-50, respectively, after 180 min of simulated sunlight illumination (Fig. S8b), which are more than an order of



magnitude lower than the cases with the presence of Pt. As the most commonly used co-catalyst in photocatalytic hydrogen production, it has been well accepted that Pt can accelerate the rate of charge transfer and act as a charge trap center, providing more active sites for photocatalytic reactions [11,12,14,16].

The stability and reusability of ECN-V<sub>N</sub>-4/C-50 was evaluated by repeating the photocatalytic hydrogen production experiments five times. No reduction in the activity of hydrogen production was observed over the five consecutive cycles (Fig. 7d), suggesting that ECN-V<sub>N</sub>-4/C-50 has excellent stability for photocatalytic hydrogen evolution. The XRD peak intensity of ECN-V<sub>N</sub>-4/C-50 decreased slightly after five use cycles (Fig. S9a), which is indicative of small deterioration in its crystallinity. This could be partially brought by the recovery of used photocatalyst and the subsequent pretreatment for instrumental analysis. In contrast, the FTIR spectrum of used ECN-V<sub>N</sub>-4/C-50 photocatalyst was essentially identical with that of the fresh one (Fig. S9b), which suggests that its structural composition remained intact. Together, the above results demonstrate that the ECN-V<sub>N</sub>-4/C-50 photocatalyst designed and prepared in this work has excellent performance in hydrogen production, and good stability and reusability as well.

### 3.3. Insights from DFT calculations

The energy bands and work functions of CN, CN-V<sub>N</sub>, and CN-V<sub>N</sub>/C photocatalysts were determined by DFT calculations. The supercell models representing CN, CN-V<sub>N</sub>, and CN-V<sub>N</sub>/C are shown on Fig. S10a-c. The calculated band gaps of CN and CN-V<sub>N</sub> were 2.446 and 2.021 eV, respectively (Fig. 8a and b), which are comparable to the results reported in the literature [55]. It is worth noting that the band gaps obtained by DFT calculations are slightly lower than the experimentally determined values, which is ascribed to the lack of precise exchange correlation function in DFT calculations and the exfoliation of CN in this work [56]. In addition, the results of DFT calculations further confirm that the nitrogen atoms at the C-N=C sites are preferentially lost, which is consistent with literature report [55]. The band gap of CN-V<sub>N</sub>/C was calculated to be 0.633 eV (Fig. 8c), which is much smaller than the measurement value for ECN-V<sub>N</sub>-4/C-50. This probably results from the fact that the amount of HMTA added during the fabrication was insufficient to form the structure shown on Fig. S10c, as well as the presence of components of ECN and ECN-V<sub>N</sub> in the three-dimensional nanostructure formed.

Fig. 8d-f show the total DOS of CN, CN-V<sub>N</sub>, and CN-V<sub>N</sub>/C for the 2s and 2p orbitals obtained by DFT calculations. The conduction band of CN was mainly composed of 2s and 2p orbitals, while its valence band was mainly composed of 2p orbitals (Fig. 8d). In addition, the partial DOS shows that there was obvious sp<sup>2</sup> hybridization of carbon and nitrogen atoms in the local area (Fig. S11a). Both the conduction band and valence band of CN-V<sub>N</sub> were composed of 2p orbitals (Fig. 8e). The partial DOS indicates that the nitrogen vacancy states were mainly contributed by C 2p orbitals (Fig. S11b), which resulted from the dangling bonds of carbon atoms at the sites of nitrogen loss. The larger DOS value of 2p orbital on CN-V<sub>N</sub>/C was mainly contributed by the C 2p orbitals (Fig. 8f and Fig. S11c), which arose from the intercalation of carbon species.

The work functions of CN, CN-V<sub>N</sub>, and CN-V<sub>N</sub>/C were calculated to be 4.782, 4.313, and 3.888 eV, respectively (Fig. 8g-i). Relative to a reversible hydrogen electrode (RHE) of 4.5 eV, their Fermi levels were calculated to be 0.282, -0.187, and -0.612 eV, respectively (Fig. 8j) [29]. Since the components of CN-V<sub>N</sub>/C were in continuous contact inside the three-dimensional nanostructure formed, the electrons of the component with higher Fermi level flowed to the one with lower Fermi level to reach the equilibrium state. As a result, electrons accumulated in the component with lower Fermi level, which is negatively charged, while the one with higher Fermi level carried positive charge, leading to BIEF formation [57]. The re-adjustment of the Fermi level caused changes in the entire band structure: both the conduction band

minimum and the valence band maximum of the component with lower Fermi level shifted upwards in parallel, while the conduction band and valence band of the component with higher Fermi level decreased to bring the Fermi levels into equilibrium alignment.

The bottom of the conduction band of CN, CN-V<sub>N</sub>, and CN-V<sub>N</sub>/C were 2.443, 1.831, and 0.621 eV, respectively (Fig. 8a-c), which indicates that the band structure of CN-V<sub>N</sub>/C rearranged after the formation of nitrogen vacancies and intercalation of carbon species. To determine the band structures of these photocatalysts, the Mott-Schottky curves were measured (Fig. S12). The conduction band potentials of CN, ECN, ECN-V<sub>N</sub>-4, and ECN-V<sub>N</sub>-4/C-50 were determined to be -1.51, -1.55, -1.19, and -1.11 V versus Ag/AgCl, corresponding to -1.31, -1.35, -0.99, and -0.91 V (vs. NHE), respectively [58]. Based on the UV-Vis DRS spectra, the band gaps of CN, ECN, ECN-V<sub>N</sub>-4, and ECN-V<sub>N</sub>-4/C-50 were 2.75, 2.98, 2.13, and 1.97 eV, respectively (Fig. 5b). Consequently, the valence band potentials of CN, ECN, ECN-V<sub>N</sub>-4, and ECN-V<sub>N</sub>-4/C-50 were 1.44, 1.63, 1.14, and 1.06 V (vs. NHE), respectively. The much lower valence band potential of ECN-V<sub>N</sub>-4/C-50 is attributed to the rearrangement of band structure due to the introduction of nitrogen vacancies and the intercalation of carbon species.

### 3.4. Mechanism of photocatalytic hydrogen production

For photocatalytic hydrogen production, three critical factors determine the activity of photocatalyst: (i) light absorption range; (ii) separation and transfer of photogenerated carriers; and (iii) amount of active sites [59]. In addition, the photogenerated carriers could easily recombine during migration over relatively long distance. To overcome these barriers, we designed and prepared a photocatalyst by exfoliating the multilayered CN into thin nanosheets (ECN), followed by introduction of nitrogen vacancies (ECN-V<sub>N</sub>) and intercalation of carbon species (ECN-V<sub>N</sub>/C). Dual BIEFs were formed in the modified CN without introducing heteroatoms due to the synergy of nitrogen vacancies and intercalation of carbon species: at the interface between ECN and ECN-V<sub>N</sub>, and that between ECN-V<sub>N</sub> and ECN-V<sub>N</sub>/C, with the directions from ECN-V<sub>N</sub> to ECN, and from ECN-V<sub>N</sub>/C to the ECN-V<sub>N</sub>, respectively, which promote the separation and transfer of photogenerated carriers. As a result of the reduced migration distance of photogenerated carriers, expanded light response range, larger specific surface area (and correspondingly more surface active sites), the migration rate of carriers in the photocatalyst is speeded up while the recombination of photogenerated carriers is minimized, which render it with excellent activity in photocatalytic hydrogen production.

As indicated by the results of XRD, FTIR, and Raman characterization, the main structure of CN remained after being exfoliated into thin nanosheets. The BET surface area of ECN was almost 5 times higher than that of CN, which provides more surface active sites for photocatalytic reactions. Furthermore, the migration distance from the sites of generation to the solid-liquid interface is significantly shorter in the thin nanosheets, which reduces the chance for the recombination of photogenerated carriers. In addition, the negative conduction band due to the quantum size effect can increase the activity of photogenerated electrons. Therefore, the photocatalytic activity of ECN in hydrogen production is greatly enhanced compared to pristine CN.

The introduction of nitrogen vacancies reduced the band gap and expanded the absorption range of visible light. Meanwhile, the introduction of nitrogen vacancies as electron or hole traps could suppress the recombination of photogenerated electron-hole pairs and optimize the original  $\pi$ -conjugate structure of ECN, which triggers the redistribution of charge and significantly promotes the participation of electrons in photocatalytic reactions. In addition, with preferential removal of three-coordinated nitrogen atoms in CN structure, the under-coordinated carbon sites that resulted from nitrogen vacancies are highly active for adsorption of reactant molecules and can activate them through promoting the transfer of photogenerated electrons from CN to the adsorbed reactant molecules for subsequent redox reactions.

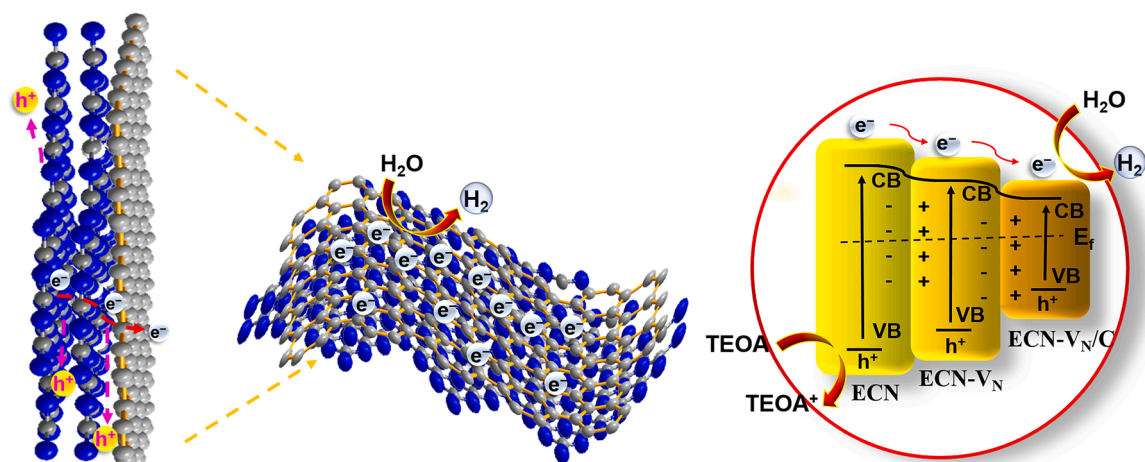


Fig. 9. Probable electron transfer pathways of photocatalytic hydrogen production in the presence of ECN-VN-4/C-50 under simulated sunlight illumination.

Nitrogen vacancies in CN were reported to be the sites responsible for the adsorption and activation of  $N_2$  [35],  $NO_x$  [60,61], and  $O_2$  [62]. In particular, they have also been found to promote the adsorption of water molecules and thus facilitate photocatalytic hydrogen production [50]. Similarly, in the photocatalytic system of this study, the nitrogen vacancies on the surface of ECN can promote the adsorption of water molecules, and thus render them easier to accept electrons to yield hydrogen. Meanwhile, the presence of excessive vacancies can also lead to narrowing of the band gap and reduction in the redox capacity of carriers, thus increasing the chance for the recombination of photo-generated carriers [35]. Therefore, the introduction of nitrogen vacancies to ECN could enhance its photocatalytic activity, but an optimal level is important for the photocatalyst's performance.

The three-dimensional hierarchical nanostructure of ECN-VN/C enables efficient light harvesting by multiple light scattering, while the greater specific surface area also provides more exposed active sites for surface reactions. Furthermore, the intercalated carbon species also improves the conductivity of the photocatalyst and facilitates the transfer of photogenerated electrons to the surface [36], which is confirmed by the photocurrent response curves and results of EIS characterization. Most importantly, the formation of nitrogen vacancies and the intercalation of carbon species between the components change the intrinsic Fermi energy level of the photocatalyst. The adjustment of the Fermi level brought by the rearrangement of the entire band structure results in a charge imbalance in the depth direction perpendicular to the interface, resulting in the formation of dual BIEFs at the interfaces of different components. As illustrated on Fig. 8j, the flow of electrons from the ECN-VN/C component to the ECN-VN component renders the latter more electronegative. As a result, a BIEF along the ECN-VN direction is developed, which greatly accelerates the migration of photo-excited electrons. Similarly, a BIEF also forms at the interface between the ECN component and the ECN-VN component, with the direction from ECN-VN to ECN.

Fig. 9 depicts the probable electron transfer pathways of sunlight photocatalytic hydrogen production in the presence of ECN-VN-4/C-50. Under normal conditions, due to the influence of energy levels, the photogenerated holes on the valence band of ECN component may migrate to the valence band of ECN-VN component, but the transfer would be restricted by the strong hindrance of the BIEF. Similar effect also exists between the CN-VN component and the CN-VN/C component in the photocatalyst. As a result, the holes can only transfer laterally in the respective layers where they are generated. With favorable band structure and dual BIEFs, the photoexcited electrons generated in all components can flow easily to the surface. In particular, the separated migration pathways of electrons and holes greatly reduce the tendency of electron-hole recombination.

#### 4. Conclusions

A high-efficiency ECN-VN/C photocatalyst was designed and fabricated by exfoliating multilayered CN into thin nanosheets, followed by introduction of nitrogen vacancies and intercalation of carbon species. The ECN-VN/C photocatalyst possesses strong light absorption capacity and a large surface area, and excellent photochemical properties. With all the three components of CN-VN/C in continuous contact inside the three-dimensional nanostructure, dual BIEFs form due to the synergy of nitrogen vacancies and intercalation of carbon species, which greatly enhance the separation and migration of photogenerated carriers. The photocatalytic hydrogen evolution rate of the prepared ECN-VN/C photocatalyst was up to 14582.1  $\mu\text{mol/g}$  after 180 min of simulated sunlight illumination, which is about 12 times higher than that of pristine CN, and it also exhibited excellent reusability and stability. This work offers a promising strategy for boosting the migration and separation efficiency of photogenerated carriers via the synergy of defect engineering and intercalation engineering.

#### CRedit authorship contribution statement

**Xue Ma:** Conceptualization, Data curation, Visualization, Methodology, Investigation, Writing – original draft. **Hefa Cheng:** Conceptualization; Funding acquisition; Supervision; Writing – original draft; Writing – review & editing.

#### Declaration of Competing Interest

The authors declare that they have no known competing financial interests or personal relationships that could have appeared to influence the work reported in this paper.

#### Acknowledgments

The constructive comments of anonymous reviewers on an earlier version of this manuscript are greatly appreciated. This work was supported in parts by the Natural Science Foundation of China (Grant Nos. 41725015 and U2006212).

#### Appendix A. Supporting information

Supplementary data associated with this article can be found in the online version at [doi:10.1016/j.apcatb.2022.121497](https://doi.org/10.1016/j.apcatb.2022.121497).

## References

- [1] Z.W. Seh, J. Kibsgaard, C.F. Dickens, I. Chorkendorff, J.K. Nørskov, T.F. Jaramillo, *Science* 355 (2017) 4998.
- [2] X. Li, J. Yu, J. Low, Y. Fang, J. Xiao, X. Chen, *J. Mater. Chem. A* 3 (2015) 2485–2534.
- [3] M.S. Faber, S. Jin, *Energy Environ. Sci.* 7 (2014) 3519–3542.
- [4] R.S. Mim, E. Sharaf Aldeen, A. Alhebshi, M. Tahir, *J. Phys. D: Appl. Phys.* 54 (2021), 503001.
- [5] Z. Xie, J. Chen, Y. Chen, T. Wang, X. Jiang, Y. Xie, C.-Z. Lu, *Appl. Surf. Sci.* 579 (2022), 152003.
- [6] Q. Lu, Y. Yu, Q. Ma, B. Chen, H. Zhang, *Adv. Mater.* 28 (2016) 1917–1933.
- [7] I. Staffell, D. Scamman, A. Velazquez Abad, P. Balcombe, P.E. Dodds, P. Ekins, N. Shah, K.R. Ward, *Energy Environ. Sci.* 12 (2019) 463–491.
- [8] S.E. Hosseini, M.A. Wahid, *Renew. Sust. Energ. Rev.* 57 (2016) 850–866.
- [9] G.L. Chiarello, M.H. Aguirre, E. Selli, *J. Catal.* 273 (2010) 182–190.
- [10] Q. Xie, Y. Wang, B. Pan, H. Wang, W. Su, X. Wang, *Catal. Commun.* 27 (2012) 21–25.
- [11] Z. Wang, C. Li, K. Domen, *Chem. Soc. Rev.* 48 (2019) 2109–2125.
- [12] S. Chen, T. Takata, K. Domen, *Nat. Rev. Mater.* 2 (2017) 17050.
- [13] J. Kibsgaard, T.F. Jaramillo, *Angew. Chem. Int. Ed.* 53 (2014) 14433–14437.
- [14] N. Fajrina, M. Tahir, *Int. J. Hydrog. Energy* 44 (2019) 540–577.
- [15] T. Hisatomi, J. Kubota, K. Domen, *Chem. Soc. Rev.* 43 (2014) 7520–7535.
- [16] I. Roger, M.A. Shipman, M.D. Symes, *Nat. Rev. Chem.* 1 (2017) 0003.
- [17] L. Zhang, C. Guo, T. Chen, Y. Guo, A. Hassan, Y. Kou, C. Guo, J. Wang, *Appl. Catal. B-Environ.* 303 (2022), 120888.
- [18] M. Zhu, S. Kim, L. Mao, M. Fujitsuka, J. Zhang, X. Wang, T. Majima, *J. Am. Chem. Soc.* 139 (2017) 13234–13242.
- [19] Y. Wu, X. Chen, J. Cao, Y. Zhu, W. Yuan, Z. Hu, Z. Ao, G.W. Brudvig, F. Tian, J. C. Yu, C. Li, *Appl. Catal. B-Environ.* 303 (2022), 120878.
- [20] J. Ran, W. Guo, H. Wang, B. Zhu, J. Yu, S.-Z. Qiao, *Adv. Mater.* 30 (2018) 1800128.
- [21] J. Liu, W. Fu, Y. Liao, J. Fan, Q. Xiang, *J. Mater. Res. Sci. Technol.* 91 (2021) 224–240.
- [22] G. Mamba, A.K. Mishra, *Appl. Catal. B-Environ.* 198 (2016) 347–377.
- [23] W. Yu, D. Xu, T. Peng, *J. Mater. Chem. A* 3 (2015) 19936–19947.
- [24] L. Chen, Y. Wang, S. Cheng, X. Zhao, J. Zhang, Z. Ao, C. Zhao, B. Li, S. Wang, S. Wang, H. Sun, *Appl. Catal. B-Environ.* 303 (2022), 120932.
- [25] J. Ran, T.Y. Ma, G. Gao, X.-W. Du, S.Z. Qiao, *Energy Environ. Sci.* 8 (2015) 3708–3717.
- [26] P. Niu, L.-C. Yin, Y.-Q. Yang, G. Liu, H.-M. Cheng, *Adv. Mater.* 26 (2014) 8046–8052.
- [27] Y. Chen, Y. Qu, P. Xu, X. Zhou, J. Sun, *J. Colloid Interface Sci.* 601 (2021) 326–337.
- [28] Z. Wang, Z. Wang, X. Zhu, C. Ai, Y. Zeng, W. Shi, X. Zhang, H. Zhang, H. Si, J. Li, C.-Z. Wang, S. Lin, *Small* 17 (2021) 2102699.
- [29] Y. Yu, W. Yan, X. Wang, P. Li, W. Gao, H. Zou, S. Wu, K. Ding, *Adv. Mater.* 30 (2018) 1705060.
- [30] F. Zhao, N. Zhang, H. Li, X. Zhang, Z. Luo, Y. Wang, *Energy Environ. Mater.* 0 (2021) 1–9.
- [31] M. Wang, G. Tan, H. Ren, A. Xia, Y. Liu, *Appl. Surf. Sci.* 492 (2019) 690–702.
- [32] P.-Y. Kuang, X.-J. Zheng, J. Lin, X.-B. Huang, N. Li, X. Li, Z.-Q. Liu, *ACS Omega* 2 (2017) 852–863.
- [33] G. Liu, G. Zhao, W. Zhou, Y. Liu, H. Pang, H. Zhang, D. Hao, X. Meng, P. Li, T. Kako, J. Ye, *Adv. Funct. Mater.* 26 (2016) 6822–6829.
- [34] J. Xu, L. Zhang, R. Shi, Y. Zhu, *J. Mater. Chem. A* 1 (2013) 14766–14772.
- [35] C. Lv, Y. Qian, C. Yan, Y. Ding, Y. Liu, G. Chen, G. Yu, *Angew. Chem. Int. Ed.* 57 (2018) 10246–10250.
- [36] H. Gao, R. Cao, S. Zhang, H. Yang, X. Xu, *ACS Appl. Mater. Inter.* 11 (2019) 2050–2059.
- [37] G. Zhang, Y. Xu, C. He, P. Zhang, H. Mi, *Appl. Catal. B-Environ.* 283 (2021), 119636.
- [38] C. Liu, W. Wang, M. Zhang, C. Zhang, C. Ma, L. Cao, D. Kong, H. Feng, W. Li, S. Chen, *Chem. Eng. J.* 430 (2022), 132663.
- [39] H. Yan, H. Yang, *J. Alloy. Compd.* 509 (2011) 26–29.
- [40] X. She, J. Wu, H. Xu, J. Zhong, Y. Wang, Y. Song, K. Nie, Y. Liu, Y. Yang, M.-T. F. Rodrigues, R. Vajtai, J. Lou, D. Du, H. Li, P.M. Ajayan, *Adv. Energy Mater.* 7 (2017) 1700025.
- [41] W. Xing, K. Cheng, Y. Zhang, J. Ran, G. Wu, *Nanomater.* -basel 11 (2021) 1480.
- [42] X. Ma, G. Wang, L. Qin, J. Liu, B. Li, Y. Hu, H. Cheng, *Appl. Catal. B-Environ.* 288 (2021), 120025.
- [43] C. Cheng, L. Mao, Z. Huang, J. Shi, B. Zheng, Y. Zhang, L. Guo, *J. Colloid Interface Sci.* 601 (2021) 220–228.
- [44] F. He, G. Chen, Y. Yu, S. Hao, Y. Zhou, Y. Zheng, *ACS Appl. Mater. Inter.* 6 (2014) 7171–7179.
- [45] A. Johansson, H.-C. Tsai, J. Aumanen, J. Koivistoinen, P. Myllyperkiö, Y.-Z. Hung, M.-C. Chuang, C.-H. Chen, W.Y. Woon, M. Pettersson, *Carbon* 115 (2017) 77–82.
- [46] Z. Mao, J. Chen, Y. Yang, D. Wang, L. Bie, B.D. Fahlman, *ACS Appl. Mater. Inter.* 9 (2017) 12427–12435.
- [47] B. Liu, L. Ye, R. Wang, J. Yang, Y. Zhang, R. Guan, L. Tian, X. Chen, *ACS Appl. Mater. Inter.* 10 (2018) 4001–4009.
- [48] B. Fahimrad, A. Asghari, M. Rajabi, *Microchim. Acta* 184 (2017) 3027–3035.
- [49] J. Li, Y. Yin, E. Liu, Y. Ma, J. Wan, J. Fan, X. Hu, *J. Hazard. Mater.* 321 (2017) 183–192.
- [50] F. Yang, H. Li, K. Pan, S. Wang, H. Sun, Y. Xie, Y. Xu, J. Wu, W. Zhou, *Sol. RRL* 5 (2021) 2000610.
- [51] Z. Zhang, L. Lu, Z. Lv, Y. Chen, H. Jin, S. Hou, L. Qiu, L. Duan, J. Liu, K. Dai, *Appl. Catal. B-Environ.* 232 (2018) 384–390.
- [52] Y. Shi, Q. Zhao, J. Li, G. Gao, J. Zhi, *Appl. Catal. B-Environ.* 308 (2022), 121216.
- [53] C. Han, L. Wu, L. Ge, Y. Li, Z. Zhao, *Carbon* 92 (2015) 31–40.
- [54] Q. Shen, N. Li, R. Bibi, N. Richard, M. Liu, J. Zhou, D. Jing, *Appl. Surf. Sci.* 529 (2020), 147104.
- [55] Q. Tay, P. Kanhere, C.F. Ng, S. Chen, S. Chakraborty, A.C.H. Huan, T.C. Sum, R. Ahuja, Z. Chen, *Chem. Mater.* 27 (2015) 4930–4933.
- [56] J. Liu, G. Wang, B. Li, X. Ma, Y. Hu, H. Cheng, *Sci. Total Environ.* 784 (2021), 147227.
- [57] X.T. Zhu, Y. Xu, Y. Cao, D.F. Zou, W. Sheng, *Appl. Surf. Sci.* 574 (2022), 151650.
- [58] C. Shan, X. Zhang, S. Ma, X. Xia, Y. Shi, J. Yang, *Colloids Surf. Physicochem. Eng. Asp.* 636 (2022), 128108.
- [59] M. Humayun, H. Ullah, A.A. Tahir, A.R. bin Mohd Yusoff, M.A. Mat Teridi, M. K. Nazeeruddin, W. Luo, *Chem. Rec.* 21 (2021) 1811–1844.
- [60] Y. Li, M. Gu, M. Zhang, X. Zhang, K. Lv, Y. Liu, W. Ho, F. Dong, *Chem. Eng. J.* 389 (2020), 124421.
- [61] J. Liao, W. Cui, J. Li, J. Sheng, H. Wang, Xa Dong, P. Chen, G. Jiang, Z. Wang, F. Dong, *Chem. Eng. J.* 379 (2020), 122282.
- [62] C. Zhou, Z. Zeng, G. Zeng, D. Huang, R. Xiao, M. Cheng, C. Zhang, W. Xiong, C. Lai, Y. Yang, W. Wang, H. Yi, B. Li, *J. Hazard. Mater.* 380 (2019), 120815.